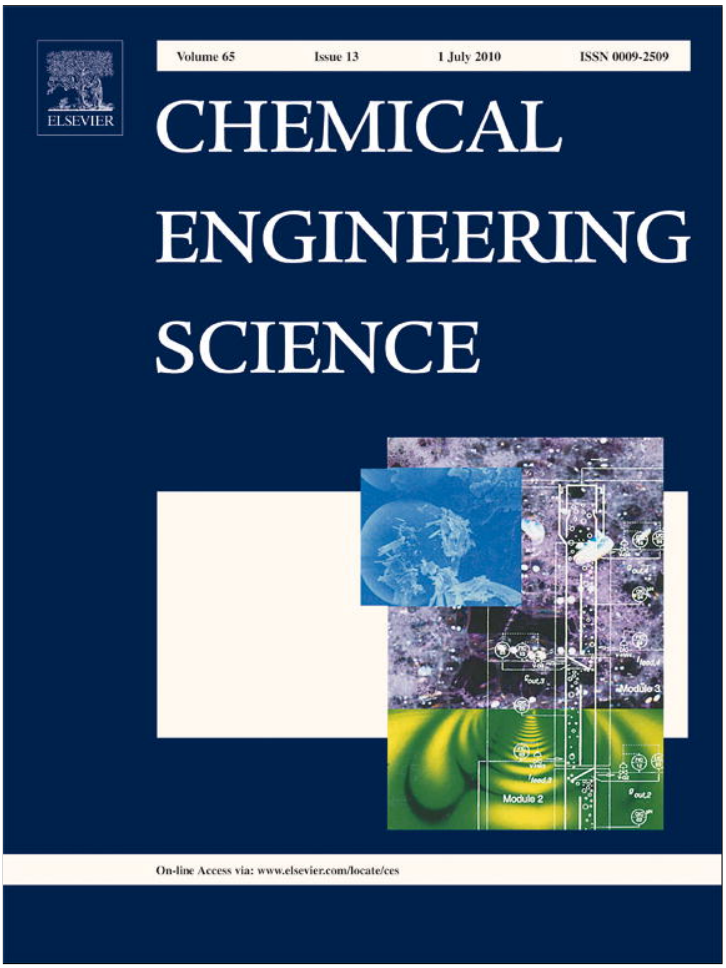

Chemical Engineering Science 65 (2010) 4046–4054

Contents lists available at ScienceDirect

Chemical Engineering Science

journal homepage: www.elsevier.com/locate/ces

Consideration of the dynamic forces during bubble growth in a capillary tube

A. Vazquez [a,*], I. Leifer [b], R.M. Sánchez [a]

[a] Universidad Autónoma Metropolitana—Iztapalapa, I.R.E. Av. San Rafael Atlixco No. 186, Col. Vicentina C.P. 09340, México, D.F., Mexico
[b] Marine Science Institute, University of California, Santa Barbara, CA 93106-5080, USA

ARTICLE INFO

Article history:
Received 1 May 2009
Received in revised form
1 December 2009
Accepted 25 March 2010
Available online 2 April 2010

Keywords:
Bubble
Bubble formation
Bubble growth
Equivalent spherical radius
Fluid dynamics
Rayleigh–Plesset

ABSTRACT

Single bubbles were generated from a capillary tube in quiescent water and the bubble formation process was studied in detail using high-speed video at two pressures, 1.38 and 0.93 kPa. The bubble equivalent spherical radius, r, was derived from the data sets of 100 bubbles: (1) the a and b semi-axes values for an ellipsoidal model and (2) a (more accurate) cylindrical integration of the bubble image in 1-pixel layers. The two methods were compared and showed a significant improvement with the more accurate integration approach. Based on the time trends in the derivatives of a and b, three growth phases were identified and the different forces acting on the bubble were calculated. The analysis showed significant differences between the two cases, despite similar times from appearance to detachment. For the 0.93 kPa case, the bubble shape detachment is described by Cassini oval while for 1.38 kPa it is a lenmiscate. For the study conditions, the momentum force was negligible for both cases; however, the viscous drag force, added mass, and surface tension forces were not. The bubble eccentricity exhibited an oscillatory behavior, which we propose arose from highly non-linear wave-phenomena. Finally, only the low-pressure case was in agreement with the predictions of Oguz and Prosperetti (1993); for flows less than the critical flow, the high pressure was not in agreement, indicating a smaller value for the transition to super-critical flow for the study conditions.

1. Introduction

Many bubble-mediated processes are strongly size dependent. Thus, the ability to precisely control and predict the size of bubbles produced in industrial processes is of great importance. Typical examples are catalyzed gas–liquid reactions—e.g., hydrogenations, oxidations, and hydroformylations, which are elaborated in bubble slurry reactors, for which bubble size and shape can strongly influence the selectivity of fast heterogeneous gas–liquid reactions (Raffensberger et al., 2005). Bubble-wake development is another important factor that is bubble-size and shape dependent (Liu et al., 2005) and can result in qualitatively different mixing characteristics in multiphase reactors (Koynov and Khinast, 2004).

Aside from bubble volume and trajectory, another important aspect of the bubble formation process is "weeping." Weeping is when liquid penetrates the capillary tube due to sharp pressure decreases in the tube after bubble detachment (McCann and Prince, 1969). Weeping can cause significant problems for the operation of distillation and absorption processes involving sieve trays (Zhang and Tan, 2000).

For these reasons, prediction of the bubble volume (V_B) at the moment it separates from an injector or orifice has received significant attention (Titomanlio et al., 1976; Clift et al., 1978; Tsuge and Hibino, 1978; Blanchard and Syzdek, 1979; Takahashi et al., 1980; Pinczewski, 1981; Miyahara et al., 1982; Gaddis and Vogelpol, 1986; Teresaka and Tsuge, 1993). A simple empirical expression has been proposed to relate the inner radius of the orifice, injector, or capillary tube (r_{cap}) to the generated bubble's equivalent spherical radius (r) for low flow rates (Padday and Pitt, 1973):

$$r = [6r_{cap}\sigma_L/g(\rho_L - \rho_G)] \quad (1)$$

where σ_L is the liquid surface tension, g is gravity and ρ_L and ρ_G are the liquid and gas densities, respectively. However, numerical and experimental studies (Ellingsen and Risso, 2001; Wu and Gharib, 2002; Tomiyama et al., 2002; Ohta et al., 2005) suggest greater complexity in the bubble formation process with V_B varying with the flow rate Q as $V_B \sim Q^{6/5}$ above a critical gas flow rate (Q_C) and equal to a characteristic volume (V_C) for $Q < Q_C$ (Oguz and Prosperetti, 1993). These predictions were obtained with a numerical model that used a boundary-integral potential-flow calculation based on the Rayleigh–Plesset equation.

In their numerical study, Oguz and Prosperetti (1993) proposed the existence of two different growth regimes as a function of Q. They proposed that formation of single bubbles or a mono-disperse bubble line required a very rapid decrease in gas

* Corresponding author.
E-mail address: zeta24_75@yahoo.com (A. Vazquez).

0009-2509/$ - see front matter © 2010 Elsevier Ltd. All rights reserved.
doi:10.1016/j.ces.2010.03.041

pressure once the bubble grows beyond V_C. In the absence of this pressure decrease, a gas jet issues from the orifice and fragments into a broad size-distribution of bubbles. Bubbles formed from this jet may coalescence and exhibit other irregularities (Leighton et al., 1991).

Another important factor in the bubble formation process arises from the bubble generation manner, which influences their size and trajectory after detachment. Wu and Gharib (2002) observed two stable shapes (spherical and ellipsoidal) depending on the way bubbles are generated. In addition, they characterized their experimental observations in terms of the Eötvös ($Eo = 4g\rho_L r_{cap}^2/\sigma_L$) and Morton ($M = g\mu_L^4(\rho_L - \rho_G)/\rho_L^2\sigma_L^3$) numbers, where μ_L is the liquid viscosity. Wu and Gharib (2002) reported very low values of M and Eo.

Experiments by Tomiyama et al. (2002) for bubbles in the range $650 < r < 3000\,\mu m$ in distilled water showed that bubble rise velocity and shape can be markedly sensitive to initial conditions—i.e., the way the bubbles were formed. They observed that when a bubble was released from a nozzle with small initial deformation, the rise velocity was low and the motion tended to be zig-zag or planar oscillatory. In contrast, when a bubble was released with large initial shape deformation, its rise velocity was faster and the motion was more likely helical. Their experiments were in a 0.2-m square by 1.0-m tall tank.

Other observations indicate that initial conditions are important. Ellingsen and Risso (2001) observed that the initial conditions of bubble separation could affect the ascending bubble trajectory. Duineveld (1995) observed two rise velocity modes for bubbles $700 < r < 1200\,\mu m$ in super-clean water, which were attributed to initial conditions. Further, numerical simulation of the motion of a gas bubble rising in a viscous liquid (Ohta et al., 2005) indicated that for rising "spherical-cap" bubbles with high Eo and low M, the initial bubble conditions and/or geometry influenced the bubble trajectory.

Many studies have analyzed bubble trajectory and shape during bubble separation from the orifice or at some distance above the orifice—e.g., Duineveld (1995), Fdhila and Duineveld (1996), Maxworthy et al. (1996), Krishna and van Baten (1999), Leifer et al. (2000), Ellingsen and Risso (2001), Wu and Gharib (2002), and Tomiyama et al. (2002). Other studies observed bubble growth and shape from appearance in the tip of an orifice or capillary tube until detachment (Kupferberg and Jamenson, 1969; Pinczewski, 1981; Gaddis and Vogelpol, 1986; Tsuge, 1986; Longuet-Higgins et al., 1991; Oguz and Prosperetti, 1993; Teresaka and Tsuge, 1993; Sundar and Tan, 1999; Loubière et al., 2003; Loubière and Hébrard, 2003, 2004). However, detailed observations of the bubble formation process from appearance at the capillary tube tip through detachment are lacking in the literature.

In this study, we present observations of the entire bubble formation process and initial dynamics. Specifically, we generated sets of 100 individual bubbles with $r = 535$ and $860\,\mu m$ at two air pressures (0.93 and 1.38 kPa), which represented the limiting pressures for the formation of single bubbles in our experimental set-up. From these data, the different forces acting on the bubbles are calculated to identify the important processes during bubble growth, and to compare with the predictions of Oguz and Prosperetti (1993).

2. Experimental set-up

In the experimental set-up (Fig. 1), the airflow Q was maintained by a pump (Cole-Parmer, Illinois, USA, Gast-SN1093) at a pressure of 12 kPa. After passing through a filter (Cole-Parmer, Illinois, USA, NOVA-Micro), airflow is controlled

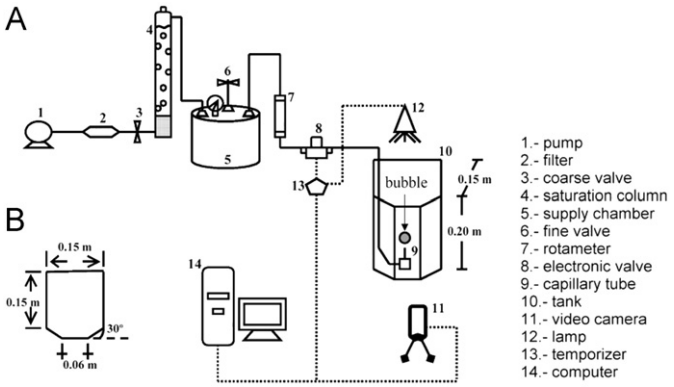

Fig. 1. (A) Schematic of experimental set-up. (B) Schematic of tank cross-section (top view).

by a coarse valve as it enters a water pre-saturation column, which prevents rapid changes in bubble volume after separation due to inflow to the bubble of water vapor (Manley, 1960). The air then enters a cylindrical supply chamber ($3.7 \times 10^{-3}\,m^3$). After the supply chamber, a fine valve reduces the pressure. The supply chamber is maintained at a constant pressure that could be varied between 0 and 4.4 kPa and was connected to a rotameter (No. 11/1–250 ml min^{-1}, Gilmont Inc., St. Louis, MO, USA). Air pulses are created by an electronic valve (PSV-1, Aalborg Corp., Orangeburg, NY, USA), connected to a glass capillary tube (Drummond Scientific, Broomall, PA, US), with an inner diameter of $990 \pm 10\,\mu m$ mounted in an acrylic base. Air travels from the rotameter to the capillary tube through a thin copper pipe with an inner diameter of $1.3 \times 10^{-3}\,m$. The capacitance number (N_C) is (Tsuge and Hibino, 1983) $N_C = V_{CH}g\rho_L/\pi r_{cap}^2 P_{OR}$, where P_{OR} is the orifice pressure and V_{CH} is the volume chamber. For our set-up, $N_C = 0.15$, which is within the range for steady flow and formation of solitary bubbles with the same volume ($N_C < 1$). Bubbles were produced in a glass ($3 \times 10^{-4}\,m$ wall thickness) hexagonal tank 0.15-m wide and deep and 0.20-m tall. Wall effects during bubble formation, separation, and acceleration within the tank were negligible (Filderis and Whitmore, 1961). Bubbles were generated every 3 min to allow liquid motions induced by the previous bubble to be damped, thereby avoiding hydrodynamic interactions other than those due to the isolated bubble motions. The tank was filled with distilled water (Thermal-Line, USA) and maintained at $22 \pm 0.5\,^{\circ}C$. The vertically oriented capillary tip was at a depth of 0.09 m.

The bubble interface was imaged by a high-speed, 8-bit gray-scale, video camera (MotionScope 8000S, Lake Image Systems, NY, USA) at 4000 frames s^{-1} and 100×98 pixel resolution. The camera used an optical array made from a Precise Eye lens (1-61453 Navitar, Rochester, NY, USA) with distortion less than 0.14% joined to a biconvex lens (KB7, Newport Corp., Irvine, USA) with a 100-mm focal length. This provided a size resolution of $590\,\mu m$ per pixel. Image quality was improved with a polarized filter (PL52mm, Kenko, Japan), which allowed brightness to be diminished at the outer edge of the images. Illumination was by an 85-Watt fluorescent lamp Reggy-Light (equivalent to a 425-Watt incandescent bulb) shining on the back wall of tank. A diffusion screen decreased small-scale inhomogeneity in the illumination. The camera, electronic valve, and fluorescent lamp were all connected to a temporizer (trigger circuit) (TI01-Hiquel, Gleichenberg, Austria). Images were recorded directly to a PC and then processed with ImageJ version 1.40f (Rasband, 1997–2008). The threshold was set slightly above the background intensity (Vazquez et al., 2005; Leifer et al., 2003).

Two data sets were collected of 100 individual air bubbles formed in water by air pulses at pressures of either 0.93 or 1.38 kPa, hereafter termed the low-pressure and high-pressure cases, respectively. Of course, for different capillary tubes, a greater range of pressures could be studied—pressures to 8 MPa are used in industrial settings (Tsuge et al, 1992). These cases represent the limiting values of our experimental set-up for single bubble generation and yielded bubble radii of 535 μm and 890 μm and $Eo=1.3$ and 3.5 for the low and high pressure cases, respectively. For the study, $M=2.4\times10^{-11}$. For this study, the water surface tension (σ_L) was 0.073 N m^{-1}, the water density ρ_L was 1000 kg m^{-3}, and the water viscosity μ_L was 0.001 kg m^{-1} s^{-1}.

The pixel resolution implies significant uncertainty at the earliest times, primarily in the values of a and b, which are not used in force calculations, but only in identifying transitions between growth phases. The variables used to calculate the forces, primarily r, are derived from integration over the entire bubble and thus are far less sensitive to pixel uncertainty. As a result, the measured values (displacement, bubble axis, bubble radius, bubble volume, etc.) agreed to better than 1–2% (standard deviation) between bubbles. All values in this study are data set averages.

3. Forces and bubble growth

Image sequences of the low and high-pressure case bubbles show significant differences during growth as well as the evolution of the bubble shape (Fig. 2). For the high-pressure case, bubbles grow larger than for the low-pressure case; however, for both cases, detachment occurred after approximately the same time period. This study investigates the underlying processes of this difference.

3.1. Bubble radius calculation

The equivalent spherical bubble radius (r_E) for an ellipsoidal bubble is (Sam et al., 1996)

$$r_E=\frac{\sqrt[3]{a^2b}}{2} \tag{1'}$$

where a and b are the vertical and horizontal axes of an ellipsoid-shaped bubble, respectively, and are measured from the image. r also was calculated from the image by vertically subdividing the image into 1-pixel thick layers, which then were integrated cylindrically by assuming radial symmetry to calculate bubble volume (V_B). The equivalent spherical bubble image-processing radius (r_{IMG}) then is calculated from V_B. Comparison of these two methods (Fig. 3) shows that assuming an ellipsoidal shape (which visually is clearly inappropriate) produces a significant overestimate of r. In this study we use r_{IMG}, hereafter referenced as r.

Although the trend in $r(t)$ (Fig. 3) is a monotonic increase without obvious inflections, the image sequence (Fig. 2) shows several shape transitions, from the Initial Phase, when the shape is controlled by surface tension and the capillary tube and is well-described as an attached sphere, to the Final Phase, when the shape is described by either a Cassini oval or a lemniscate for the low and high-pressure cases, respectively (Vazquez et al., 2005). During the Transition Phase between the Initial and Final Phases, the bubble exhibits shape irregularities, e.g., 1.75–2.75 ms in the low and high-pressure cases, respectively use of respectively not clear (see Fig. 2). For the high-pressure case, the bubble actually becomes bullet-shaped during a process termed "flattening." The "sharp edges" or high frequency components of the interface are highly suggestive of a non-linear wave process, discussed further below. The three different bubble growth phases, termed the Initial (I), Transition (II), and Final (III) Phases, were identified from the minima in ε and the trends in da/dt and db/dt (Fig. 4). Interestingly, bubble eccentricity exhibits an oscillatory behavior.

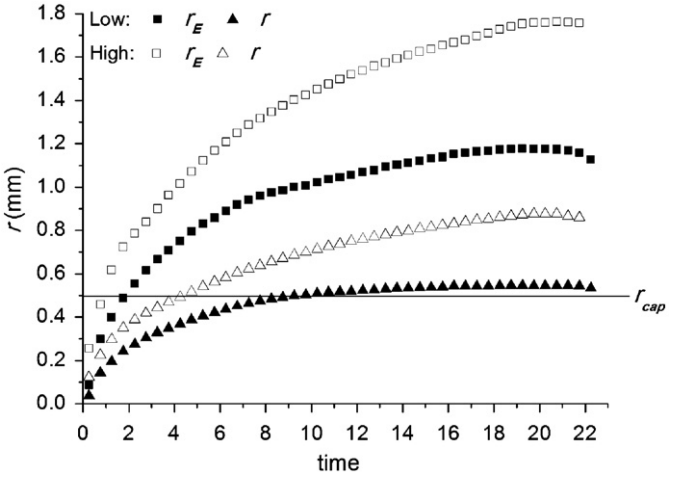

Fig. 3. The equivalent spherical radius calculated for an ellipsoid (r_E), and for image symmetry (r) with respect to time during bubble growth for low and high-pressure cases demonstrating the error from approximating a growing bubble as an ellipsoid. Data key on figure.

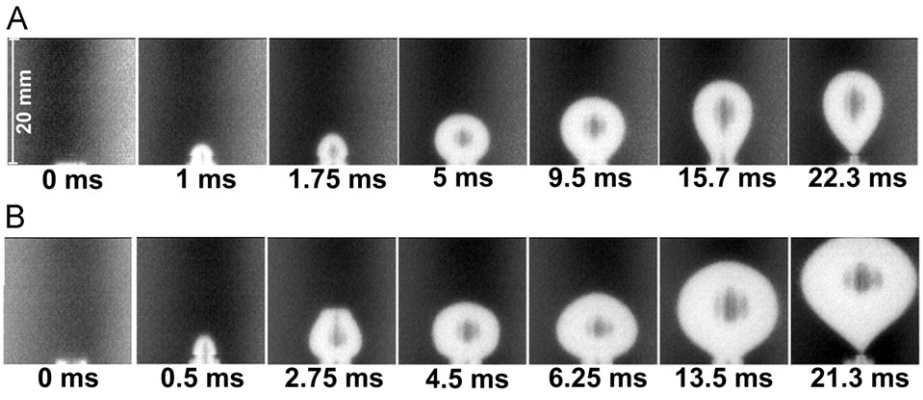

Fig. 2. Negative image sequence of bubble growth showing the different shape evolution for (A) low and (B) high-pressure cases. Time and length scales noted on figure. Time is relative to bubble appearance at the capillary tip. The original camera image resolution was interpolated from 100 × 98 pixels to 800 × 784 pixels for these images.

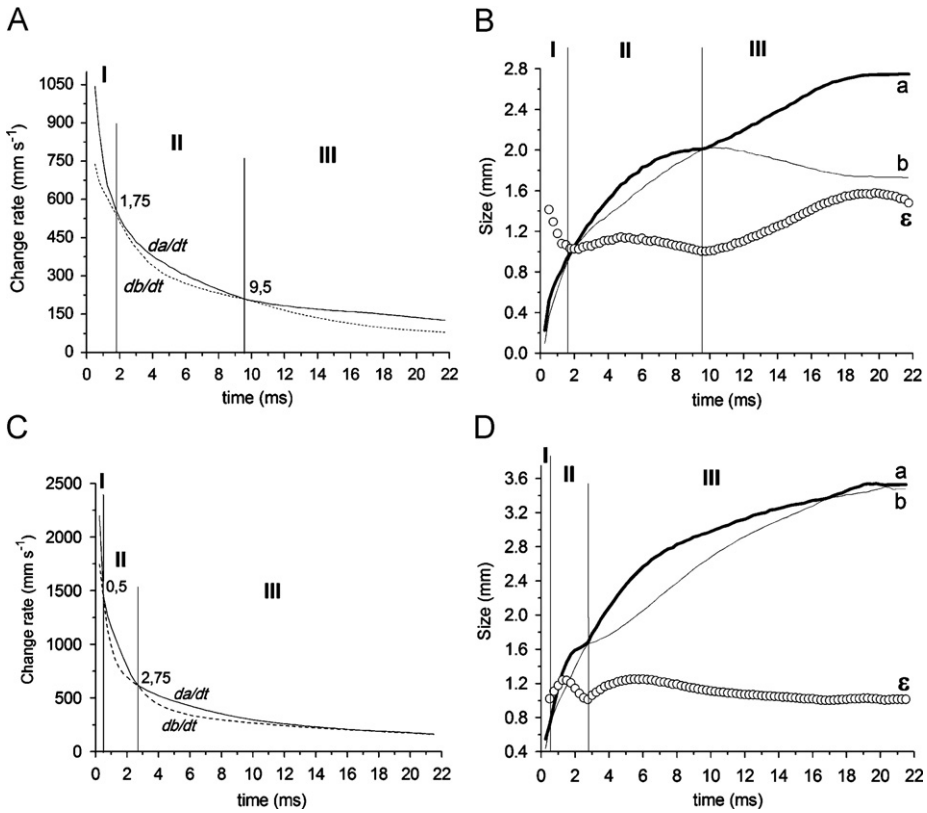

Fig. 4. Low and high pressure-cases. (A–C) Differential evolution of the axes (da/dt) and (db/dt). (B–D) Time evolution of the vertical (a) and horizontal (b) axes and the bubble eccentricity (ε), respectively. Trends in a and b were used to identify the different growth phases.

3.2. Bubble forces

A bubble's time history during formation is determined by the balance of forces on the bubble and capillary tip. The forces in the rise (vertical) direction acting on a bubble are illustrated in Fig. 5.

The buoyancy force (F_B) is (Teresaka and Tsuge, 1993)

$$F_B = g(\rho_L - \rho_G)V_B \tag{2}$$

where the bubble volume is $V_B = 4/3\ \pi r^3$ with $\rho_G \ll \rho_L$. The gas momentum force (F_M) results from gas momentum through the orifice and is (Martín et al., 2006)

$$F_M = \frac{\rho_G}{\pi r_{cap}^2}\left(\frac{dV_B}{dt}\right)^2 \tag{3}$$

where t is time. The surface tension force (F_S) is (Duhar and Colin, 2006)

$$F_S = \frac{2\pi r_{cap}^2 \sigma_L}{r} \tag{4}$$

The viscous drag force (F_D) prior to detachment primarily is determined by growth of bubble's vertical mass centroid (dY_{CM}/dt) (Zhang and Shoji, 2001):

$$F_D = -\frac{1}{2}\pi\rho_L C_D r^2\left(\frac{dY_{CM}}{dt}\right)^2 \tag{5}$$

where C_D is the drag coefficient and for Reynolds number (Re) between 277 and 633 is $2r\rho_L\ (da/dt)/\mu_L$ (Martin et al., 2006) and using $r = r_{IMG}$, $C_D = 15.34/Re + 2.163/Re^{0.6}$ (Nahra and Kamotani, 2003).

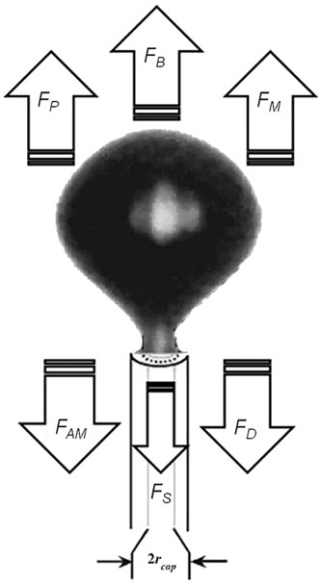

Fig. 5. Schematic showing the vertical forces on a bubble during formation from a capillary tip.

The added mass force (F_{AM}) is (Li et al., 2002)

$$F_{AM} = -\frac{d}{dt}\left[\left(\rho_G + \frac{11}{16}\rho_L\right)V_B\frac{dY_{CM}}{dt}\right] \tag{6}$$

and arises from bubble growth and the resultant displacement of the surrounding fluid. Thus, F_{AM} is the liquid's resistance to bubble interface changes.

Finally, the pressure force (F_P) is (Kasimsetty, 2008)

$$F_P = \pi r_{cap}^2 \left(\frac{2\sigma}{r} - 2\rho_L g r \right) \quad (7)$$

Based on the data for $r(t)$, the time evolution of the forces in Eqs. (2)–(7) was calculated for the two pressure cases (Figs. 6 and 7). Then, the bubble forces were analyzed with respect to time and changes in $a(t)$ and $b(t)$, which are proxies for bubble shape (Figs. 3 and 4), because they depend in part on the values of a and b and hence ε· Note, the forces do not balance (sum to zero), because the bubble is growing. The sum, F_S+F_P, is shown because these two forces are close to balanced for both pressure cases.

For the low-pressure case (Fig. 6), during the Initial (I) Phase, ε decreases to a local minima and the predominant forces (other than the closely balanced F_S and F_P forces) are F_D and F_{AM}, both of which rapidly increased in magnitude, reaching a peak between 0 and 0.5 ms (Fig. 6B). The combination F_S+F_P is $-2\rho_L g r$ and thus always is negative and small due to the bubble's small size and strong curvature. After reaching a maximum, F_{AM} approximately stabilizes, decreasing very gradually until the end of the Initial Phase, while F_D decreases rapidly. During the Initial Phase, which lasts 1.75 ms, the bubble shape is nearly spherical (Fig. 2A), with a slightly greater than b (Fig. 4B).

During the Transition (II) Phase, ε remains nearly constant and the bubble is close to spherical (Fig. 2A), i.e., $\varepsilon \sim 1.0$ (Fig. 4B), with a slight vertical elongation (a becomes greater than b) (Fig. 4B). Onset of this phase corresponds to an increase in the rate of decrease of F_{AM}, while F_D continues to decrease (Fig. 6B). The bubble elongation arises because the negative vertical forces (F_{AM} and F_D) decrease while F_B increases monotonically (Fig. 4B). The Transition Phase lasts until 9.5 ms.

The Final (III) Phase, which lasts until bubble separation at 22.5 ms, begins when ε reaches a second minimum of 1 and corresponds to a shift to a slower growth rate of F_B. During this phase, ε increases, reaching a maximum slightly before separation. The increase in ε occurs due to a decrease in b and an increase in a. During this phase, the magnitudes of F_{AM} and F_D decrease towards zero, eventually becoming less in magnitude than F_B prior to separation. Note, F_M is negligible for the low-pressure case for all three phases.

For the high-pressure case, the growth phases are more difficult to distinguish from the trends in $a(t)$ and $b(t)$, than for the low pressure case (Fig. 3); however, $\varepsilon(t)$ shows an even stronger, non-linear oscillatory behavior than for the low-pressure case (Fig. 4). However, da/dt and db/dt show clear changes in slope that are very similar to the slope changes in da/dt and db/dt in the low-pressure case, which were used to identify the growth phases (Fig. 4C). Transitions between the Initial, Transition, and Final Phases were identified at 0.5 and 2.75 ms, respectively. The bubble forces for the high-pressure case are shown in Fig. 7.

During the Initial (I) Phase, other than the closely balanced F_S and F_P forces, the dominant forces are F_D and F_{AM}, the same as for the low-pressure case. Both forces grow rapidly until reaching a peak between 0 and 0.5 ms at the end of this phase (Fig. 7B), decreasing thereafter until separation. Note, F_S and F_P are even more closely balanced than for the low-pressure case. As in the low-pressure case, the momentum force is negligible for all growth phases.

During the Transition (II) Phase, ε rapidly increased to a maximum of 1.23, and then decreased to a minimum of 1.0 at the end of the phase. Towards the end of this phase, however, the vertical growth slows dramatically, leading to a decrease in da/dt

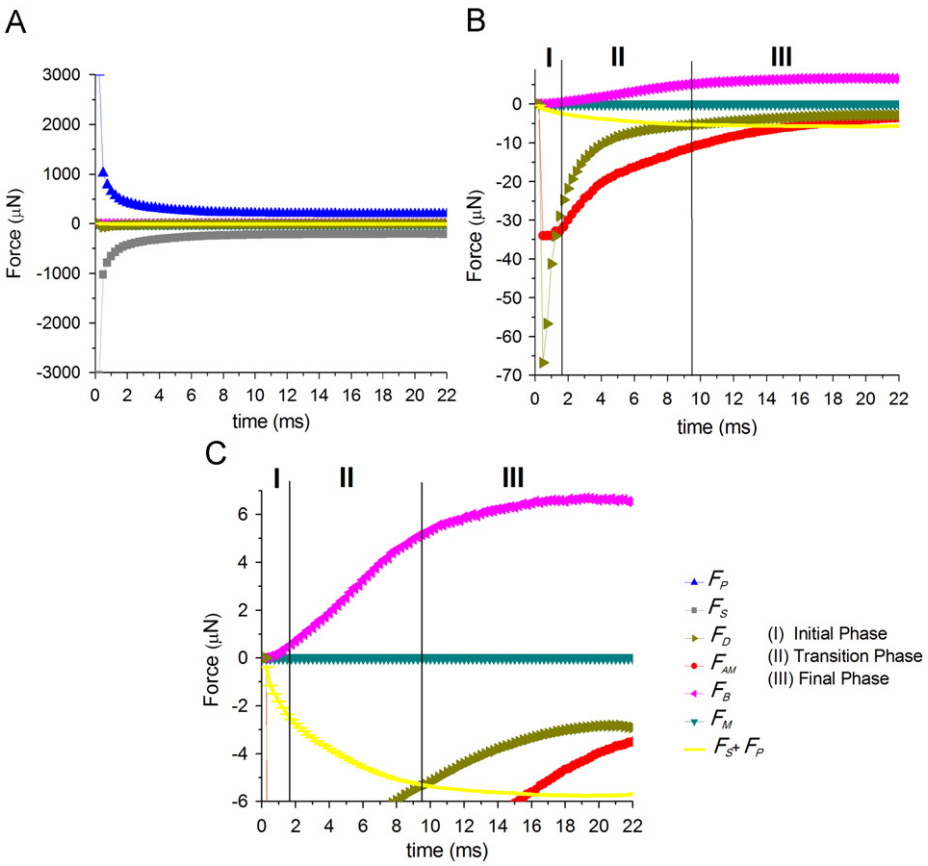

Fig. 6. (A) Forces acting on the bubble for the low pressure-case; (B) and (C) show enlarged view. Legend on (C).

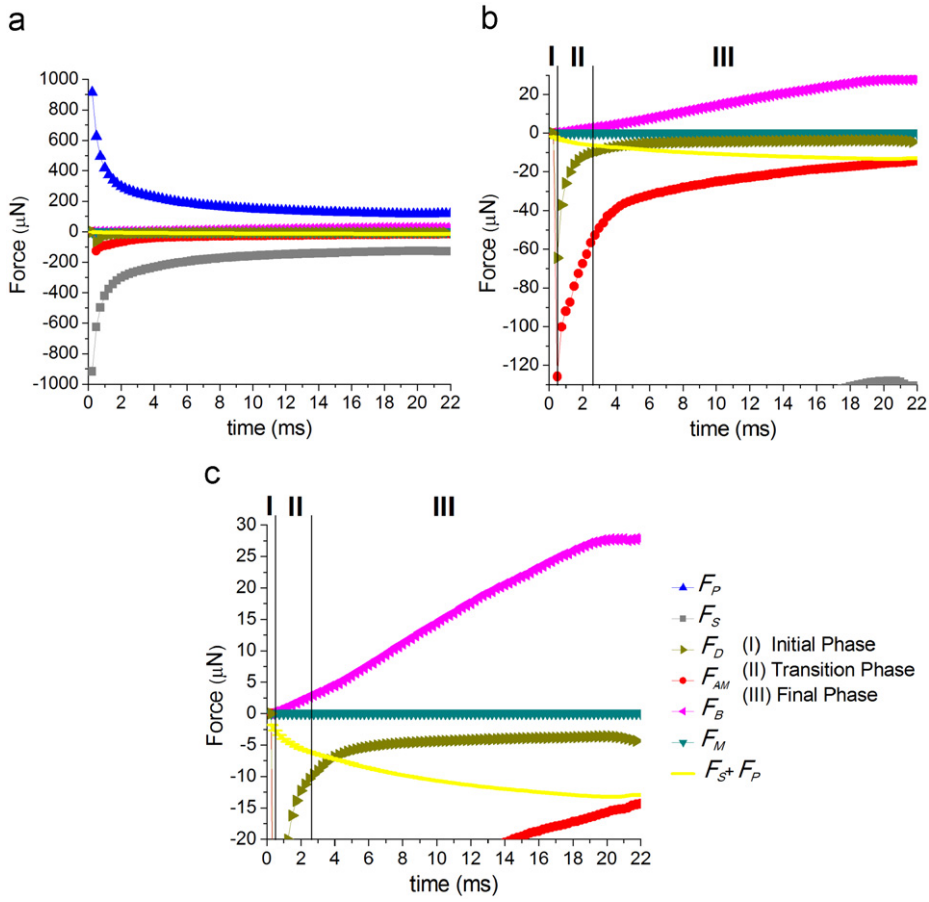

Fig. 7. (A) Forces acting on the bubble for the high-pressure case; (B) and (C) show enlarged view. Legend on (C).

(Fig. 4C) and a phenomenon termed "flattening," in which the bubble becomes bullet-shaped (Fig. 2B), Flattening corresponds to the decrease of ε towards a minimum of 1.0. During this phase, F_B increased monotonically, eventually becoming non-negligible, although it is far from dominant. The rapid increase in F_{AM} and F_D during the Initial Phase ceased at the beginning of the Transition Phase, decreasing thereafter. During the Transition Phase, F_D decreased more rapidly than F_{AM} although F_{AM} always remains larger than F_D.

During the Final (III) Phase, ε first increased from a minimum of 1.0 to a maximum of 1.25 at $t=6$ ms, and then very gradually decreased with t (Fig. 4). There also was an acceleration in the growth of F_B at ~6 ms. F_B eventually becomes greater than F_D, F_{AM}, and F_S+F_P just before bubble detachment. The balance between F_S and F_P continues shifting in favor of F_S (with a 12.5 μN difference as the bubble becomes larger) corresponding to a period where ε lies in the range 1.06–1.01, i.e., seemingly nearly spherical, although the bubble shape is far better described as a lemniscate prior to detachment (Fig. 2B).

4. Bubble generation flow regimes

The high and low-pressure cases produced significantly different final bubble volumes despite similar formation times and identical capillary tube diameter; thus r upon detachment cannot be described by the simple relationship in Eq. (1). Oguz and Prosperetti (1993) proposed that bubble formation was different for bubbles smaller and larger than a characteristic bubble radius (r_C):

$$r_C = \left(\frac{3\sigma_L r_{cap}}{2g\rho_L}\right)^{1/3} \tag{8}$$

They indicated that the bubble's buoyancy is sufficiently strong to detach only when $r > r_C$ with r at detachment proportional to $Q^{6/5}$. In contrast, for small Q, $r < r_C$, and the bubble detaches when $r \approx r_C$. They further assume that all bubbles with $r < r_C$ detach from the needle with the same r irrespective of Q.

For this study ($r_{cap}=0.495$ mm) bubbles generated at low and high pressures detached with $r=0.535$ and 0.860 mm, respectively, both of which were significantly less than the calculated $r_C=1.76$ mm. Yet, for our experiments, V_B grew approximately linearly with respect to Q only for the high-pressure case (Fig. 8).

5. Discussion

5.1. Critical radius

Oguz and Prosperetti (1993) proposed that if during the formation process and prior to separation, r increases to larger than orifice radius (r_{cap}), the pressure in the bubble becomes progressively higher than the value needed to ensure quasi-equilibrium of the gas–liquid interface. In such case, bubble growth proceeds dynamically, unlike where the pressure allows quasi-equilibrium of the interface. Where r_{cap} is very small (0.1–2 mm), this overpressure is large and further growth occurs very rapidly, as if a gas jet issued from the needle. The difference between these two bubble growth modes is that Oguz and

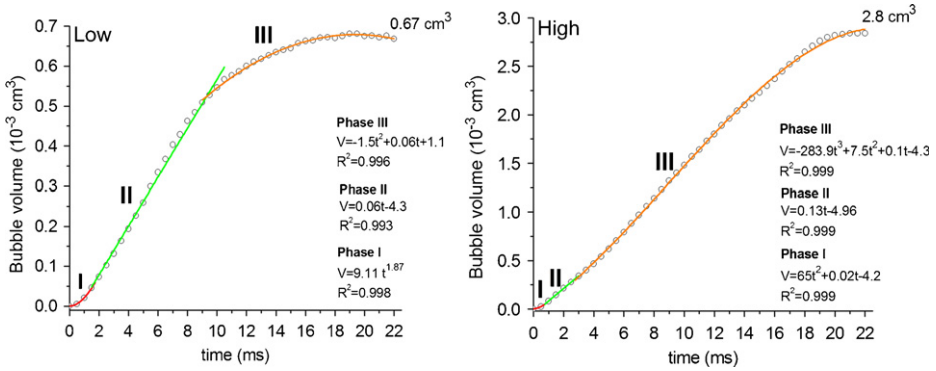

Fig. 8. Bubble volume, V_B, evolution with time, t, for both pressure cases, and three-part fits to data (least squares and reduced Chi-square) over the range showed. The value of V_B for the low-pressure case reached near steady state, while the high pressure case did not. Data key on figure.

Prosperetti (1993) propose that for $Q < Q_C$, there is a rapid decrease in bubble pressure once the bubble has grown larger than r_{cap}, while for $Q > Q_C$ it is not. For the low-pressure case our observations are in agreement with the predictions of Oguz and Prosperetti (1993) for $Q < Q_C$. Specifically, the increase in r largely ceased shortly after the bubble reached r_{cap} (Fig. 3) at 9.3 ms, only a few milliseconds prior to the beginning of the final phase at 9.5 ms. The low-pressure bubble only grew 8% larger than r_{cap}.

In addition Oguz and Prosperetti (1993) considered that the limiting growth factor is the gas mass supply rather than the inertia forces (F_{AM} and F_D) and that the initial transient phase, when surface tension and inertial forces are important, is brief and can be neglected. This implies that the dominant forces during bubble growth are buoyancy, surface tension, and hydrodynamic forces, while the drag force was assumed negligible.

In contrast, our data showed that bubble growth for the high-pressure case increased at a rapid rate until r was significantly larger than r_{cap} (volume grows linearly with time—until ~20 ms). Because Q is constant, pressure changes in the capillary tube must explain the difference in growth patterns. With respect to the Oguz and Prosperetti (1993) model, our data support the existence of two different growth regimes. These regimes may be unrelated to r_C, or else the value of r_C could be about half that proposed by Oguz and Prosperetti (1993). One possible explanation is that Oguz and Prosperetti (1993) made several simplifications. They neglected the drag force and assumed that the initial transient phase (when F_S and F_{AM} are important) is brief. With respect to our observations, the drag force, while small, never becomes negligible. Note that this conclusion is appropriate because F_S+F_P are closely balanced, and thus we consider only the remaining forces. Also, the initial transient phase is significant for the low-pressure case (~9.5 ms), and even for the high-pressure case where the combined Initial and Transient Phases last ~2.75 ms, more than 10% the bubble lifetime, and a period when significant bubble growth occurs. Finally, the spherical shape assumed for calculation of r (Oguz and Prosperetti 1993) creates a bias towards larger r (Fig. 3).

The buoyancy force decreases for the low-pressure case or abruptly stabilizes for the high-pressure case for the last few milliseconds prior to detachment. Thus, the proposed pressure decrease for sub-critical bubble growth (bubble detachment where $r \approx r_C$) is unlikely to have occurred for the high-pressure case, which had not reached quasi-equilibrium. For the low-pressure case, there is a minimal decrease in r, and thus no evidence of a decrease in pressure. Thus, any pressure drop must have occurred across the capillary needle or in the pressure chamber. During this time, r decreases notably, or slightly, for the low and high-pressure cases, respectively. Thus, during this period, there must be either an increase in the bubble pressure or a decrease in the flow. Note, because r is calculated by a layer integration approach, significant shape changes do not introduce errors into r, which are apparent in Fig. 3 for an ellipsoid (or worse spherical) assumption and in the comparison between the high and low-pressure cases.

For the high-pressure case, there is a rapid but small decrease in r for the last few milliseconds, which is very poorly characterized by r derived from a best-fit ellipsoid. Other than the rapid change in F_B, there is a significant increase in F_D for both high and low pressure cases. These changes are driven by the rapid chance in shape accompanying the bubble beginning to pinch-off, which causes a reversal of bubble growth. Interestingly, in both pressure cases, the balance between F_S and F_P achieves steady state in the low-pressure case, and decreases slightly for the high-pressure case. This suggests that balance between these two forces is important to determining the growth behavior of the bubble—where not stabilized, the bubble r grows as $Q^{6/5}$; else the bubble detaches when $r \approx r_C$.

5.2. Significant forces during bubble growth

For both cases, the gas momentum force (F_M) was at most 0.02% of F_D, and thus was negligible. This is in agreement with other studies, which have argued F_M can be treated as negligible in numerical bubble dynamics models (Kupferberg and Jamenson, 1969; Pinczewski, 1981). In contrast, for the low-pressure case, F_{AM} and F_S+F_P ranged between 5–51% and 0.6–9% of F_D, respectively. Clearly they were important (non-negligible) to the bubble formation process for the study conditions. For the high-pressure case, F_{AM} and F_S+F_P ranged between 22–195% and 3–20% of F_D, respectively.

Other researchers have investigated the forces governing bubble growth. Loubière et al. (2003) generated air bubbles in water using a perforated single orifice in a solid stainless steel tube, in which bubble adhesion to the orifice surface was observed. Note that for this formation mechanism, the surface contact angle is important, unlike that for the capillary tube formation used herein. For their study, the orifice radius was 0.35 mm, $r \sim 2500\,\mu m$, and $Q = 2–4\,\mu m^3\,s^{-1}$. They calculated that the viscous drag and the gas momentum forces were negligible (about 0.1–1 μN) throughout bubble growth; in contrast, they found that the buoyancy, surface tension, and added mass forces (about 100 μN) were dominant. They indicated that during the bubble's initial growth the bubble vertical expansion is retarded because of the high liquid inertia; then, the F_{AM} decreases to a minimum at ~15 ms. Q for Loubière et al. (2003) was significantly greater than in our study where $Q = 0.03$ and $0.14\,\mu m^3\,s^{-1}$ for the low- and high-pressure cases, respectively. Thus, the final r in this

study was smaller. Also, Loubière et al. (2003) do not indicate how they calculated r. Our approach used a layer volume method that avoids the over-estimation of bubble size in an ellipsoidal bubble shape approach. Despite these differences, our bubble forces for the low-pressure case, F_D, F_{AM}, and F_B, are in the same range of magnitude as for Loubière et al. (2003).

Several recent numerical studies have investigated the forces acting on the bubble during growth. In some studies, some forces were neglected. In a numerical study, Zhang and Tan (2000) neglected F_S and F_D for air bubbles in water with $Re \sim 10^3$–10^4 based on a comparison between their model and the experimental results of McCann and Prince (1969). However, results from this study show that it can be inappropriate to neglect F_S and F_D—e.g., for higher Re, $1.1 \times 10^6 < Re < 1.8 \times 10^6$.

5.3. Bubble shape irregularity during formation

The formation phases were selected based on trends in da/dt and db/dt, i.e., the relative growth rates of the two axes. In the high-pressure case, these shifts are readily apparent in the image sequence (Fig. 2), which shows sharp shape changes such as elongation and flattening, followed by slow growth towards a lemniscate. These processes are less readily apparent in the low-pressure case image sequence; however, trends in ε, da/dt, and db/dt show the same oscillatory pattern, discussed below. Thus, we propose that the underlying processes responsible for this oscillatory behavior evolve far faster for the high-pressure than the low-pressure case. It is important to note that because the bubble shape is poorly described by an ellipsoid (e.g., Fig. 3), a and b are poor indicators of interfacial shape, although the correlation between shifts in the forces (calculated from r) and the trend in a and b indicate they were a good proxy for the purposes in this study.

Bubble eccentricity exhibited a non-linear, oscillatory behavior, which also showed in the growth rates of a and b. These oscillations were clearly related to the flattening phenomena (Fig. 2), which appears to be part of a standing wave. The oscillatory behavior also appears related to a restoration force opposing the initial rapid growth. The initial interface growth is very rapid and likely very highly sheered. In this regard, it may have similarities with microbreaking phenomena (Banner and Phillips, 1974), where non-linear growth of interfacial instabilities leads to turbulence. In the case of bubble formation, an interfacial wave is formed that creates the "flattening;" however, because the "jet-like" nature of the initial growth decreases rapidly as the bubble becomes larger, it is rapidly damped.

6. Conclusions

This work indicates that bubble-force analysis is an important tool for understanding bubble generation and to analyze the effect of bubble shape evolution during bubble growth. Our results demonstrate that bubble size is sensitive to the manner of bubble generation and not only to capillary diameter. We found that the drag and added mass forces cannot be neglected during bubble growth; only the momentum force was negligible for our study conditions (high Re), in contrast to the conclusions of Oguz and Prosperetti (1993). Also, the assumption of bubble ellipsoidal shape is inappropriate and leads to an overestimate of bubble size, which may play a role in explaining why the two pressure cases in this study demonstrate a transition from sub-critical to super-critical flow behavior for bubble formation despite the high pressure bubble being smaller than the critical flow proposed by Oguz and Prosperetti (1993). Other reasons for the discrepancy could result from Oguz and Prosperetti (1993) neglecting the drag and inertial forces, assuming the initial and transition phases are very rapid, and assumptions of laminar flow in the capillary needle. Future work should focus on the non-linear oscillatory behavior observed in the bubble eccentricity and its coincidence with the bubble growth regimes. Future work also could investigate where bubble formation occurs at faster than single rates, and from plates and irregular surfaces.

Nomenclature

a	major bubble axis (cm)
b	minor bubble axis (cm)
C_D	drag coefficient (dimensionless)
Eo	Eötvös number (dimensionless)
F_{AM}	added mass force (N)
F_B	buoyancy force (N)
F_D	viscous drag force (N)
F_M	momentum force (N)
F_P	pressure force (N)
F_S	surface tension force (N)
g	gravity ($cm\,s^{-2}$)
Q	flow rate ($cm^3\,s^{-1}$)
Q_C	critical flow rate ($cm^3\,s^{-1}$)
M	Morton number (dimensionless)
N_C	capacitance number (dimensionless)
P_{OR}	orifice pressure (Pa)
r	bubble radius (cm)
r_{IMG}	image processing radius (cm)
r_E	equivalent spherical radius. (cm)
r_{cap}	capillary internal radius (cm)
r_C	critical radius (cm)
Re	Reynolds number
V_B	bubble volume (cm^3)
V_C	characteristic bubble volume (cm^3)
V_{CH}	chamber volume (cm^3)
t	time (s)
Y_{CM}	vertical mass centroid (cm)
ε	eccentricity (dimensionless)
μ_L	liquid viscosity ($kg\,m^{-1}\,s^{-1}$)
σ_L	liquid surface tension (cp)
ρ_L	liquid phase density ($g\,cm^3$)
ρ_G	gas phase density ($g\,cm^3$)

Acknowledgements

The authors gratefully acknowledge Prof. Elizabeth Salinas and Alberto Soria for the equipment and financial support, and the support of UC MEXUS.

References

Banner, M.L., Phillips, O.M., 1974. On the incipient breaking of small scale waves. J. Fluid Mech. 65, 647–656.
Blanchard, D.C., Syzdek, L.D., 1979. Production of air bubbles a specified size. Chem. Eng. Sci. 32, 1109–1112.
Clift, R., Grace, J.R., Weber, M.E., 1978. Bubbles, Drops and Particles. Academic Press, London.
Duhar, G., Colin, C., 2006. Dynamics of bubbles growth and detachment in a viscous shear flow. Phys. Fluids 18, 77–101.
Duineveld, P.C., 1995. The rise velocity and shape of bubbles in pure water at high Reynolds number. J. Fluid Mech. 292, 325–332.
Ellingsen, K., Risso, F., 2001. On the rise of an ellipsoidal bubble in water: oscillatory paths and liquid-induced velocity. J. Fluid Mech. 440, 235–268.
Fdhila, R.B., Duineveld, P.C., 1996. The effect of surfactant on the rise of a spherical bubble at high Reynolds and Peclet numbers. Phys. Fluids 8 (2), 310–321.

Filderis, V., Whitmore, R.L., 1961. Experimental determination of the wall effect for spheres falling axially in cylindrical vessels. Br. J. Appl. Phys. 12, 490–497.
Gaddis, E.S., Vogelpol, A., 1986. Bubble formation in quiescent liquids under constant flow conditions. Chem. Eng. Sci. 41, 97–105.
Kasimsetty, S.K., 2008. Theorical modeling and correlational analysis of single bubble dynamics from submerged orifices liquid pools. MS University of Cincinnati Engineering: Mechanical Engineering.
Koynov, A., Khinast, J.G., 2004. Effects of hydrodynamics and Lagrangian transport on chemically reacting bubble flows. Chem. Eng. Sci. 59, 3907–3927.
Krishna, R., van Baten, J.M., 1999. Rise characteristics of gas bubbles in a 2D rectangular column: VOF simulations versus experiments. Int. Commun. Heat Mass Transfer 26, 965–974.
Kupferberg, A., Jamenson, G.J., 1969. Bubble formation at a submerged orifice above a gas chamber of finite volume. Trans. Inst. Chem. Engrs. 47, 241–250.
Leifer, I., Patro, R.K., Bowyer, P., 2000. A study on the temperature variation of rise velocity for large clean bubbles. J. Atmos. Ocean. Technol. 17 (10), 1392–1402.
Leifer, I., De Leeuw, G.D., Kunz, G., Cohen, L., 2003. Calibrating optical bubble size by the displaced mass method. Chem. Eng. Sci. 58 (23/24), 5211–5216.
Leighton, T.G., Fajan, K.J., Field, J.E., 1991. Acoustic and photographic studies of injected bubbles. Eur. J. Phys. 12, 77–85.
Li, H.Z., Mouline, Y., Midoux, N., 2002. Modelling the bubble formation dynamics in non-Newtonian fluids. Chem. Eng. Sci. 57, 339–346.
Liu, Z., Zheng, Y., Jia, L., Zhang, Q., 2005. Study of bubble induced flow structure using PIV. Chem. Eng. Sci. 60, 3537–3552.
Longuet-Higgins, M.S., Kerman, B.R., Lunde, K., 1991. The release of air bubbles from an underwater nozzle. J. Fluid Mech. 230, 365–390.
Loubière, K., Hébrard, G., 2003. Bubble formation from a flexible hole submerged in an inviscid liquid. Chem. Eng. Sci. 58, 135–148.
Loubière, K., Hébrard, G., Guiraud, P., 2003. The dynamics of bubble growth and detachment from rigid and flexible orifices. Can. J. Chem. Eng. 81, 499–507.
Loubière, K., Hébrard, G., 2004. Influence of liquid tension (surfactants) on bubble formation at rigid and flexible orifices. Chem. Eng. Proc. 43, 1361–1369.
McCann, D.J., Prince, R.G.H., 1969. Bubble formation and weeping at a submerged orifice. Chem. Eng. Sci. 24, 801–814.
Manley, D., 1960. Change of size of air bubbles in water containing a small dissolved air content. Br. J. Appl. Phys. 11, 38–42.
Martín, M., Montes, J.F., Galán, M.A., 2006. Numerical calculation of shapes and detachment times of bubbles generated from a sieve plate. Chem. Eng. Sci. 61, 363–369.
Maxworthy, T., Gnann, C., Kürten, M., Durst, F., 1996. Experiments on the rise of air bubbles in clean viscous liquids. J. Fluid Mech. 321, 421–441.
Miyahara, T., Tanimoto, M., Takahashi, T., 1982. Bubble formation from an orifice at high injection rates—the size of bubbles above an orifice. Kagaku Kogaku Ronbunshu 8 (3), 304–306.
Nahra, K.H., Kamotani, Y., 2003. Prediction of bubble diameter at detachment from a wall orifice in liquid cross-flow under reduced and normal gravity conditions. Chem. Eng. Sci. 58, 55–69.
Oguz, H.N., Prosperetti, A., 1993. Dynamics of bubble growth and detachment from a needle. J. Fluid Mech. 257, 111–145.
Ohta, M., Imura, T., Yhosida, Y., Sussman, M., 2005. A computational study of the effect of initial bubble conditions on the motion of a gas bubble rising in viscous liquids. Int. J. Multiphase Flow 31, 223–237.
Padday, J.F., Pitt, A.R., 1973. The stability of axisymmetric menisci. Philos. Trans. R. Soc. Lond. A (275), 489–528.
Pinczewski, W.V., 1981. The formation and growth of bubbles at a submerged orifice. Chem. Eng. Sci. 36, 405–411.
Raffensberger, J.A., Glasser, B.J., Khinast, J.G., 2005. Analysis of heterogeneously catalyzed reactions close to bubbles. AIChE 51 (5), 1482–1496.
Rasband, W.S., 1997–2008. ImageJ. US National Institutes of Health, Bethesda, MD, USA, 〈http://rsb.info.nih.gov/ij/〉.
Sam, A., Gomez, C.O., Finch, J.A., 1996. Axial velocity profiles of single bubbles in water/frother solutions. Miner. Process. 47, 177–196.
Sundar, R., Tan, R.B.H., 1999. A model for bubble-to-jet transition at a submerged orifice. Chem. Eng. Sci. 54, 4053–4060.
Takahashi, T., Miyahara, T., Senzai, S., Terakado, H., 1980. Bubble formation at submerged nozzles in cocurrent, countercurrent and cross-current flow. Kagaku Kogaku Ronbunshu 6 (6), 563–569.
Teresaka, K., Tsuge, H., 1993. Bubble formation under constant-flow conditions. Chem. Eng. Sci. 48, 3417–3422.
Titomanlio, G., Rizzo, G., Acierno, D., 1976. Gas bubble formation from submerged orifices—simplified model for predicting bubble volume. Quaderni Dell Ingegnere Chimico Italiano 12 (4), 112–117.
Tomiyama, A., Celata, G.P., Hosokawa, S., Yoshida, S., 2002. Terminal velocity of single bubbles in surface tension force dominant regime. Int. J. Multiphase Flow 28, 1497–1519.
Tsuge, H., 1986. Hydrodynamics of bubble formation from submerged orifice. In: Cheremisinoff (Ed.), Encyclopaedia of fluid mechanics, vol. 43. Gulf Publishing Corporation, Houston, TX, pp. 191–232 (Chapter 4).
Tsuge, H., Hibino, S., 1978. Bubble formation from a submerged single orifice accompanied by pressure fluctuations in gas chamber. J. Chem. Eng. Jpn. 11 (3), 173–178.
Tsuge, H., Hibino, S., 1983. Bubble formation from an orifice submerged in liquids. Chem. Eng. Commun. 22, 63–79.
Tsuge, H., Nakajima, Y., Teresaka, K., 1992. Behavior of bubbles formed from a submerged orifice under high system pressure. Chem. Eng. Sci. 47, 3273–3280.
Vazquez, A., Sanchez, R.M., Salinas-Rodríguez, E., Soria, A., Manasseh, R., 2005. A look at three measurement techniques for bubble size determination. Exp. Therm. Fluid Sci. 30, 49–57.
Wu, M., Gharib, M., 2002. Experimental studies on the shape and path of small air bubbles rising in clean water. Phys. Fluids 14, 49–52.
Zhang, L., Shoji, M., 2001. Aperiodic bubble formation from a submerged orifice. Chem. Eng. Sci. 56, 5371–5381.
Zhang, W., Tan, R.B.H., 2000. A model for bubble formation and weeping at a submerged orifice. Chem. Eng. Sci. 55, 6243–6250.